Design and Control of a Novel Omnidirectional Dynamically Balancing Platform for Remote Inspection of Confined and Cluttered Environments

Matthew T. Watson[1], Daniel T. Gladwin, Tony J. Prescott, and Sebastian O. Conran

Abstract— **Remote inspection is a long standing field of interest for robotics researchers, in which robots are used to undertake inspection tasks in environments too hazardous or inaccessible to be directly entered by a human. Recent advances in grid-scale battery storage have created a new set of unique hazardous indoor spaces with characteristics unsuitable for the deployment of existing teleoperated inspection robots. This paper outlines the problems encountered in these new environments, analyses existing approaches to robotic platform design, and proposes a better suited novel platform design, based on a dynamically balancing arrangement of Mecanum wheels. Its inverse kinematic and dynamics models are developed, a proof of concept prototype is constructed, and a constrained predictive controller is derived from the developed model. Experimental results demonstrate the efficacy of this new concept.**

I. Introduction

Remote inspection has long been a staple topic of robotics researchers, with advancements in this field enabling the undertaking of inspection tasks within environments too hazardous or inaccessible to be directly entered by a human.

This particular robot was inspired by the challenges associated with the remote inspection of the Willenhall 2MW Battery Energy Storage Demonstrator in the UK[1]. This is a facility designed to provide rapid response grid storage, using a combination of chemical battery and flywheel energy storage. The battery component of this facility is composed of multiple rows of 2.4 meter high racks of lithium cells, separated by narrow access gantries. This provides perfectly acceptable access for a human, however as this too hazardous during live operation it would be desirable to be able to perform physical cell inspection using a teleoperated platform. Additionally, being a research facility, these gantries are often cluttered with additional equipment and tools, further limiting the navigable floor area. This specification leads us to require a robotic platform that is capable of achieving a height of 2.4m, whilst maintaining a minimum navigable width in the region of 0.2m in order to navigate a cluttered gantry.

Existing terrestrial remote inspection platforms can typically be grouped into two sets; those that utilise some form of wheel to provide motion, and those that use legs. Legged robots perform well on unconstrained rough terrain, can travel omnidirectionally, and provided a good approach to dealing with the cluttered navigation required by this brief, however, they are mechanically complex, expensive, and are currently still a technology in its infancy. Wheeled robots on the other hand are comparatively mechanically simple, inexpensive, and perform well on flat indoor terrain. Some wheel designs allow for omnidirectional motion, such as the Mecanum wheel (Figure 1) and the ball wheel [2]. This simplicity and reliability makes a wheeled solution superior in this application, with the omnidirectional wheel designs most suitable due to their superior manoeuvrability in confined spaces.

Consideration must also be given as to the stability of a platform. Statically stable platforms avoid toppling during acceleration or disturbance by possessing a wheel base with three or more widely spaced contact points, producing a polygon shaped footprint[7]. As long as a vertical line drawn through the stationary platform's center of mass intersects this polygon, the platform will always return to the stable upright equilibrium. As the height of the center of mass increases, a smaller range of angles from the vertical equilibrium can be attained without moving outside of this polygon, and similarly reducing the spacing of a platform's contact points reduces the range of angles over which it is stable. This gives a platform a minimum footprint width to height ratio that must be maintained to ensure a suitable degree of static stability required to resist expected acceleration and ground unevenness. Applying this logic to a robot capable of achieving this specification's maximum height of 2.4m with sufficient static stability begins to push the minimum footprint width of the robot larger than our maximum of 0.2m.

One method of reducing this wheel base whilst maintaining height is to reduce the number of contact points. Reducing to two contact points, to produce a wheeled inverted pendulum [1], reduces the contact polygon to a contact line, with the minimum platform width limited only by wheel diameter. This results in an unstable system, so energy must be continuously expended in order to dynamically balance. However, whilst this does allow the creation of a tall platform with a thin footprint, the nonholonomic constraints imposed by the two wheels typically used on this style of platform prevent the platform from travelling in a direction perpendicular to its thinnest dimension. This means the navigation of a

*This work was supported by Consequential Robotics Ltd (CqR) and the Engineering and Physical Sciences Research Council [grant number EP/M508135/1]

[1]Matthew Watson is with the Department of Electronic and Electrical Engineering, University of Sheffield, UK m.t.watson@sheffield.ac.uk

[1]www.sheffield.ac.uk/creesa/willenhall

978-1-5090-4974-5/18/$31.00 ©2018 IEEE

Fig. 1. Mecanum wheel

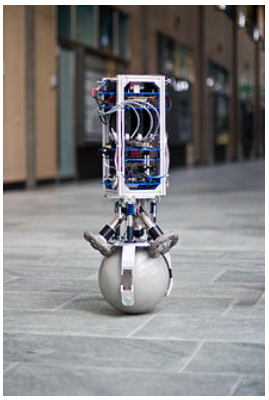

Fig. 2. ETH Zurich's Rezero Ballbot

gap smaller than the distance between the platform's wheels will require a multi-point manoeuvre, with the number of points increasing as the robot width approaches that of the gap to be navigated.

Reducing to a single contact point overcomes this limitation, giving a platform that must dynamically balance in two axes, but is able to move omnidirectionally. Ball balancing robots are the main example of this group of platforms, in which a robot with three or more omnidirectional wheels balances on top of a ball [4], shown in Figure 2, although hopping robots have also been demonstrated. The need to balance in two axes however increases the power required to maintain stability, gives a platform that must continually exhibit variations in its position in two directions rather than just one, and limits the maximum yaw torque to that which can be communicated to the floor by the friction generated by the small ball contact area twisting against the ground.

As none of these existing platform designs meet the specification described above, this paper proposes a novel platform configuration in Section II, develops its inverse kinematic and dynamics models in Section III, and uses these to implement a model predictive controller on a proof of concept prototype in Section IV. Finally, in Section V experimental results demonstrate the accuracy of the developed model, showing this new platform design is capable of meeting this application's specification.

II. Concept

The prototype in this paper presents a novel method of achieving omnidirectional motion in a smaller footprint than existing platforms, whilst still being able to produce considerable torques about the yaw axis and only needing to dynamically balance in a single axis.

This was achieved using four Mecanum wheels, arranged in two sets of two, in which one wheel in each set is the mirror image of the other taken along the shared rotation axis. These are attached to four motors, with all four axles sharing the same rotational axis. We refer to this as the Collinear Mecanum Drive (CMD).

A literature review found only one previous example of the CMD concept [5], in which three Mecanum wheels are used, with the middle wheel offset from the centre of the platform. This author successfully demonstrated dynamically balanced omnidirectional motion, however the platform exhibited poor control, taking sixty seconds to perform a 0.3m lateral translation, producing a large amount of unwanted longitudinal motion in the process. Additionally, this three wheeled design possesses a number of disadvantages compared to the four-wheeled concept presented in this paper.

Foremost, using three wheels instead of four asymmetrically distorts the set of forces the platform can produce, resulting in anisotropic mobility. This is evident in that when moving in one diagonal direction work is done by two motors coupled to the ground by two wheels, whereas in the opposite diagonal only one wheel and one motor are able to contribute to motion. This also means that when the platform produces a purely lateral net force, the two identical wheels can only be operated at half their maximum traction, as the single unique opposite wheel has to simultaneously counter the unwanted longitudinal force component of both other wheels. While the four wheeled concept presented in this paper also possesses a degree of anisotropic mobility, the set of achievable forces is symmetrical about the longitudinal axis, simplifying trajectory planning and control.

Secondly, a fourth wheel adds redundancy against wheel slip. Two different slip scenarios could occur when traversing with three wheels; if the unique centre wheel enters a slip state, there is no other wheel to provide the counterforce required to produce lateral motion. This will remove the platform's ability to traverse, rendering the platform immobile unless inertia or a longitudinal motion allows grip to be re-established. Conversely, if one of the two identical wheels were to slip whilst traversing, while the robot could still produce sideways motion, it would lose control of its attitude about the vertical axis. This occurs as when only two wheels are contacting the ground it is the same motor inputs that produce both lateral force and yaw torque, resulting in an indeterminate combination of the two. In practice this will cause the platform to follow a meandering path instead of a straight line.

There is also no evidence in the literature of either an inverse kinematic or dynamics model of this type of platform for any number of wheels, therefore one is developed and presented here.

III. Inverse Kinematics & Dynamics Model

In order to derive the inverse kinematics and nonlinear dynamics model of the proposed platform, the nonholonomic constraints introduced by the Mecanum wheels must first be derived.

Consider the proposed CMD platform depicted in Figure 3 on a flat plane, where $\{E, \hat{e}_x, \hat{e}_y, \hat{e}_z\}$ denotes the fixed reference frame, $\{B, \hat{b}_x, \hat{b}_y, \hat{b}_z\}$ represents the body attached frame obtained by rotating E about $\hat{e_z}$ by ϕ, such that $\hat{e}_z = \hat{b}_z$, with B located on the wheel rotation axis in the center of the platform, and $\{P, \hat{p}_x, \hat{p}_y, \hat{p}_z\}$ represents the pendulum attached frame obtained by rotating B about $\hat{b}_x$ by θ_p, centered at the pendulum CoM, with associated

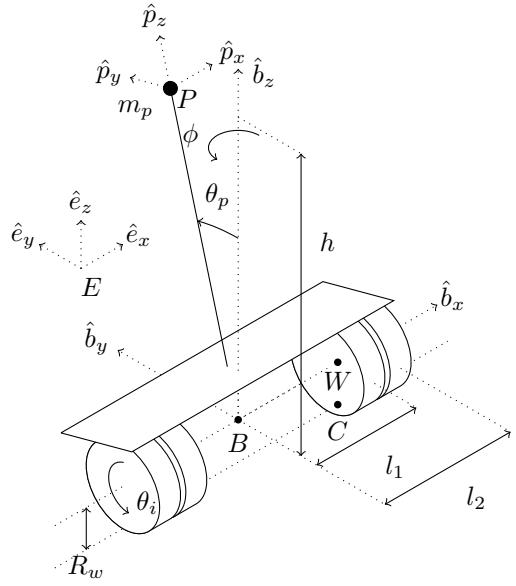

Fig. 3. CMD coordinate systems

mass m_p and inertia tensor $I_p = diag(\begin{bmatrix} I_{px} & I_{py} & I_{pz} \end{bmatrix})$. Wheel positions are defined as a rotation about $\hat{p}_x$ by θ_i. For simplicities sake only one roller is considered per wheel, and this is assumed to be positioned directly under the center of the wheel along the $\hat{e}_z/\hat{b}_z$ axis, with the contact point between this and the ground assumed to also be fixed under the center of the roller, and with the roller axis of rotation defined as a rotation of $\hat{b}_x$ by α_i about $\hat{b}_z$.

Considering one wheel independently, let $\hat{\mu}_p$ represent the unit vector running through the roller rotation axis, let W represent the wheel's centre, and let the roller contact the ground directly under W at C, where $C = W - R_w\hat{b}_z$, where R_w represents the wheel radius measured to the roller contact point.

For no slip to occur, the component of the roller's velocity at the contact point along the $\hat{\mu}_p$ direction must equal 0, so

$$\vec{v}_C \bullet \hat{\mu}_p = 0 \tag{1}$$

The velocity at C is the velocity of the wheel at W summed with the velocity due to the sum of wheel and pendulum rotation $\dot{\theta}_i + \dot{\theta}_p$, so

$$\vec{v}_C = \vec{v}_W - R_w\hat{b}_y(\dot{\theta}_i + \dot{\theta}_p) \tag{2}$$

similarly, $\vec{v}_W$ can be defined in terms of the body velocity $\vec{v}_B$, giving

$$\vec{v}_W = \vec{v}_B + \dot{\phi}l_i\hat{b}_y \tag{3}$$

where l_i represents the offset of W from B along $\hat{b}_x$.

Combining equations (1-3) and splitting $\vec{v}_B$ into its components $\vec{v}_B = \begin{bmatrix} \dot{x} & \dot{y} & \dot{z} \end{bmatrix}^T$ gives the nonholonomic constraint equation.

$$\dot{x}\cot(\alpha_i) + \dot{y} + \dot{\phi}l_i - R_w(\dot{\theta}_i + \dot{\theta}_p) = 0 \tag{4}$$

This can be applied to wheels 1 through 4 and rewritten to define the platform's inverse kinematic mapping

$$\begin{bmatrix} \dot{\theta}_1 \\ \dot{\theta}_2 \\ \dot{\theta}_3 \\ \dot{\theta}_4 \end{bmatrix} = \frac{1}{R_w}\begin{bmatrix} \cot(\alpha_1) & 1 & l_2 & -R_w \\ \cot(\alpha_2) & 1 & l_1 & -R_w \\ \cot(\alpha_3) & 1 & -l_1 & -R_w \\ \cot(\alpha_4) & 1 & -l_2 & -R_w \end{bmatrix}\begin{bmatrix} \dot{x} \\ \dot{y} \\ \dot{\phi} \\ \dot{\theta}_p \end{bmatrix} \tag{5}$$

There exist two methods of developing a dynamics model subject to these nonholonomic constraints; the Euler-Lagrange equation can be used with Lagrangian multipliers to directly incorporate the nonholonomic constraints, or the constraints can be approximately 'holonomised' using the psuedo-inverse of the inverse kinematic transformation matrix, allowing the use of the regular Euler-Lagrange equation. Zimmerman compared both methods and found their result to be identical [8].

For this paper the former approach is taken [3], deriving the overall system dynamics using the Euler-Lagrange equation in terms of j generalised coordinates and r Lagrange multipliers, defined as

$$\frac{d}{dt}\left(\frac{\partial L}{\partial \dot{q}_j}\right) - \frac{\partial L}{\partial q_j} = Q_j + \lambda_r M(q_j) \tag{6}$$

where $q_j = \begin{bmatrix} x & y & \phi & \theta_p & \theta_1 & \theta_2 & \theta_3 & \theta_4 \end{bmatrix}^T$, Q_j represents the generalised forces, and λ_r represents the Lagrange multipliers.

The constraint equation matrix M is defined as

$$M(q_j)\dot{q}_j = 0 \tag{7}$$

giving

$$M(q_j) = \begin{bmatrix} \cot(\alpha_1) & 1 & l_2 & -R_w & \\ \cot(\alpha_2) & 1 & l_1 & -R_w & [-R_w I_{4\times4}] \\ \cot(\alpha_3) & 1 & -l_1 & -R_w & \\ \cot(\alpha_4) & 1 & -l_2 & -R_w & \end{bmatrix} \tag{8}$$

L represents the total energy of the system $L = K - U$, where K represents the sum of translational and rotational kinetic energy, and U the total potential energy.

The rotational kinetic energy of the system is defined as

$$K_{rot} = \frac{1}{2}\vec{\omega}_p^T I_p \vec{\omega}_p + \frac{1}{2}\sum_{i=1}^{4}\vec{\omega}_{w,i}^T I_w \vec{\omega}_{w,i} \tag{9}$$

where

$$\vec{\omega}_{w,i} = \begin{bmatrix} \dot{\theta}_i + \dot{\theta}_p & 0 & \dot{\phi} \end{bmatrix}^T \quad \vec{\omega}_p = R_{b\to p}\vec{\omega}_b + \theta_p\hat{p}_z \tag{10}$$

in which I_w and I_p represent the wheel and pendulum inertia tensors, and $R_{b\to p}$ represents the $b \to p$ rotation matrix.

Translational kinetic energy is defined as

$$K_{trans} = \frac{1}{2}\vec{v}_p^T m_p \vec{v}_p + \frac{1}{2}m_w\sum_{i=1}^{4}\vec{v}_{w,i}^T\vec{v}_{w,i} \tag{11}$$

where

$$\vec{v}_p = R_{b\to p}\vec{v}_b + \vec{\omega}_p \times -h\hat{p}_z \quad \vec{v}_{w,i} = \vec{v}_b + \vec{\omega}_b \times l_i\hat{b}_x \tag{12}$$

Finally, potential energy is defined as

$$U = m_p g h \cos(\theta_p) \tag{13}$$

The generalised coordinates can then be derived individually as

$$\frac{d}{dt}\left(\frac{\partial L}{\partial \dot{x}}\right) - \frac{\partial L}{\partial x} = \sum_{i=1}^{4} \lambda_i \cot(\alpha_i) \tag{14}$$

$$\frac{d}{dt}\left(\frac{\partial L}{\partial \dot{y}}\right) - \frac{\partial L}{\partial y} = \sum_{i=1}^{4} \lambda_i \tag{15}$$

$$\frac{d}{dt}\left(\frac{\partial L}{\partial \dot{\phi}}\right) - \frac{\partial L}{\partial \phi} = \lambda_1 l_2 + \lambda_2 l_1 - \lambda_3 l_1 - \lambda_4 l_2 \tag{16}$$

$$\frac{d}{dt}\left(\frac{\partial L}{\partial \dot{\theta}_b}\right) - \frac{\partial L}{\partial \theta_p} = \sum_{i=1}^{4} \left\{-R_w \lambda_i - \tau_i + k_v \dot{\theta}_i\right\} \tag{17}$$

$$\frac{d}{dt}\left(\frac{\partial L}{\partial \dot{\theta}_i}\right) - \frac{\partial L}{\partial \theta_i} = \tau_i + \lambda_i R_w \sin(\alpha_i) \quad i = [1 \dots 4] \tag{18}$$

where τ_i represents a motor drive torque on wheel i.

Eliminating the four Lagrangian multipliers by substituting (18) into (14-17), expanding differentials, and eliminating $\dot{\theta}_i$ by substitution with (4) yields four ODEs representing the dynamics of the system in terms of $\zeta = (x, y, \phi, \theta_p)$, which can be arranged into the nonlinear input-affine form

$$M\ddot{\zeta} + F(\zeta, \dot{\zeta}) = H\tau_i \tag{19}$$

where

$$M = \begin{bmatrix} m_p + 4m_w + \frac{I_{wx}}{{R_w}^2} \sum_{i=1}^{4} \cot(\alpha_i)^2 & \frac{I_{wx}}{{R_w}^2} \sum_{i=1}^{4} \cot(\alpha_i) & N & 0 \\ \frac{I_{wx}}{{R_w}^2} \sum_{i=1}^{4} \cot(\alpha_i) & \frac{4I_{wx}}{{R_w}^2} + m_p + 4m_w & 0 & 0 \\ N & 0 & P & 0 \\ 0 & h_p\, m_p \cos\theta_p & 0 & 0 \end{bmatrix}$$

$$N = h_p m_p \sin(\theta_p) + \frac{I_{wx}}{{R_w}^2}\left[l_1(\cot(\alpha_2) - \cot(\alpha_3)) + l_2(\cot(\alpha_1) - \cot(\alpha_4))\right]$$

$$P = 4I_{wz} + 2\left(m_w + \frac{I_{wx}}{{R_w}^2}\right)\left({l_1}^2 + {l_2}^2\right) + I_{pz}\cos^2(\theta_p) + \sin^2(\theta_p)(I_{py} + {h_p}^2 m_p)$$

$$F(\zeta, \dot{\zeta}) = \begin{bmatrix} 0_{3\times 1} \\ \frac{1}{2}\dot{\phi}^2 \sin(2\theta_p)\left[(I_{p,z} - I_{p,y}) - h_p^2 m_p\right] \dots \\ \quad -g h_p m_p \sin(\theta_p) - \dot{\phi}\dot{x} h_p m_p \cos(\theta_p) \end{bmatrix}$$

$$H = \begin{bmatrix} \cot(\alpha_1)/R_w & \cot(\alpha_2)/R_w & \cot(\alpha_3)/R_w & \cot(\alpha_4)/R_w \\ 1/R_w & 1/R_w & 1/R_w & 1/R_w \\ l_2/R_w & l_1/R_w & -l_1/R_w & -l_2/R_w \\ -2 & -2 & -2 & -2 \end{bmatrix}$$

Examining $F(\dot{\zeta})$ shows that all of the system's nonlinearity originates in the θ_p state, and around the stationary upright equilibrium the majority of this originates in the $-g h_p m_p \sin(\theta_p)$ term.

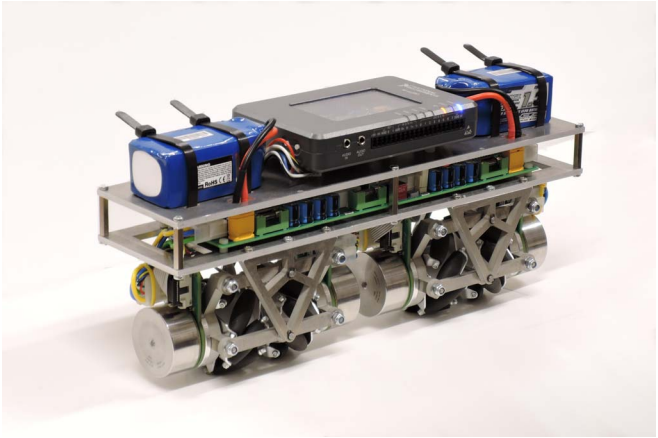

Fig. 4. Proof-of-concept prototype

This model can be linearised about the stationary upright position to give a linear state space model of the form

$$A = \begin{bmatrix} 0_{4\times 4} & I_{4\times 4} \\ \begin{bmatrix} 0 \dots & 0 \\ 0 \dots & 0 \\ 0 \dots & A_{6,4} \\ 0 \dots & A_{8,4} \end{bmatrix} & 0_{4\times 4} \end{bmatrix} \quad B = \begin{bmatrix} 0_{4\times 4} \\ \begin{bmatrix} B_{5,1} & B_{5,2} & B_{5,3} & B_{5,4} \\ h & h & h & h \\ m & n & -n & -m \\ p & p & p & p \end{bmatrix} \end{bmatrix}$$

$$C = I_{8\times 8} \quad D = 0$$

Remark 1: For $\alpha_i = \pm\left[\pi/4 \ -\pi/4 \ -\pi/4 \ \pi/4\right]^T$ *it is found that* $B_{5,i} = \pm\left[r \ -r \ -r \ r\right]^T$*, whereas for* $\alpha_i = \pm\left[\pi/4 \ -\pi/4 \ \pi/4 \ -\pi/4\right]^T$ *it is found that* $B_{5,1} = -B_{5,4}$*,* $B_{5,2} = -B_{5,3}$*, and* $|B_{5,1}| < |B_{5,2}|$*. This suggests that the optimal platform features a wheel configuration in which the two middle-most wheels share the same handedness, as this yields an equal contribution to* $\ddot{x}$ *from each wheel, whereas an asymmetric* α_i *vector results in extra emphasis being placed on the inner two wheels.*

Examining the rank of the controllability matrix of the linearised model indicates all states of the linearised model are controllable, and the observability matrix indicates there are no unobservable states.

The model parameters were populated mostly by direct measurement, with grey-box least-squares fitting used to estimate the remaining unmeasurable parameters. Wheel inertia I_{wx} was estimated by suspending a wheel freely and injecting a square wave torque input, producing a zero mean triangular angular velocity profile suitable for fitting with the ideal model of a rotating mass. The height of the pendulum's center of mass h_p was estimated by inverting the platform and suspending it by its wheels, allowing the fitting of the impulse disturbance response of θ_p to the nonlinear model of a pendulum with a friction term $-k_v\dot{\theta}_p$.

IV. Proof of Concept & Control Design

A proof of concept prototype was developed to demonstrate the real-world feasibility of this type of platform,

and to validate the model developed above. This was constructed around four Maxon brushless motors, controlled by a National Instruments myRIO. Sensing was performed using four incremental encoders, three gyroscopes, and three accelerometers. This data is fused using a 9 state Extended Kalman Filter, allowing the estimation of the two unmeasured velocity and three gyroscope bias states.

The linearised plant is found to have eigenvalues with positive real components, meaning the plant is open loop unstable. Designing model predictive controllers for open loop unstable systems is known to lead to difficulties in defining a numerically well conditioned prediction model [6], as a highly divergent step response combined with a large prediction horizon can result in a large difference in magnitude between the upper and lower rows of the prediction matrices, which when manipulated can lead to loss of precision due to the limitations of embedded floating-point arithmetic. This phenomena was observed in practice when attempting to apply MPC methods directly to the open loop plant, so the linearised plant is first compensated by a discrete infinite horizon linear-quadratic regulator with gain K, derived for state variable weights $Q = diag\left(\begin{bmatrix}0.2 & 1 & 1 & 0 & \dots & 0\end{bmatrix}\right)$ and manipulated variable weights $R = I_{4\times4}$. This approach to the prediction of unstable plants is referred to as the closed-loop paradigm [6]. The new model eigenvalues were found to possess purely negative real components, indicating exponential stability.

A dual-mode model predictive controller was designed based on this compensated model in order to apply constraints to the optimal LQR controlled system, with the MPC output c_k used to deviate the unconstrained optimal output u_k in order to maintain input and state constraint satisfaction. Additionally, the plant model was redefined in terms of deviations $\hat{x}_k$ and $\hat{u}_k$ from the steady state values x_{ss} and u_{ss}, given by $\hat{x}_k = x_k - x_{ss}$, $\hat{u}_k = u_k - u_{ss}$. These steady state values are defined by solving the simultaneous equations $x_{ss} = Ax_{ss} + Bu_{ss}$ and $y_{ss} = r_{k+1} = Cx_{ss}$.

This allows the definition of the control law

$$u_{k+i} = -K(\hat{x}_{k+i} - x_{ss}) + u_{ss} + c_{k+i} \qquad i \leq n_c \quad (20)$$

$$u_{k+i} = -K(\hat{x}_{k+i} - x_{ss}) + u_{ss} \qquad i > n_c \quad (21)$$

where n_c represents the horizon over which perturbations are included, and in which x_{ss} and u_{ss} are recalculated for every change in setpoint. The same Q and R matrices were used to define the cost function

$$J = \sum_{i=1}^{\infty} \hat{x}_{k+1+i}^T Q \hat{x}_{k+1+i} + \hat{u}_{k+i}^T R \hat{u}_{k+i} \quad (22)$$

which through substitution and Lyapunov analysis can be redefined in terms of the perturbation term c_k in a form suitable for numerical solution by a quadratic program solver. Constraints were applied to τ_i and θ_p, projected to the infinite horizon using standard MCAS approaches [6] to give a constraint polytope of the form $F_x x_k + F_c \underset{\rightarrow}{c}_k + F_r r_{k+1} \leq d$. The QP problem can now be defined as

$$\min_{\underset{\rightarrow}{c}_k} J = \underset{\rightarrow}{c}_k^T S \underset{\rightarrow}{c}_k \quad s.t.\ F_x x_k + F_c \underset{\rightarrow}{c}_k + F_r r_{k+1} \leq d \quad (23)$$

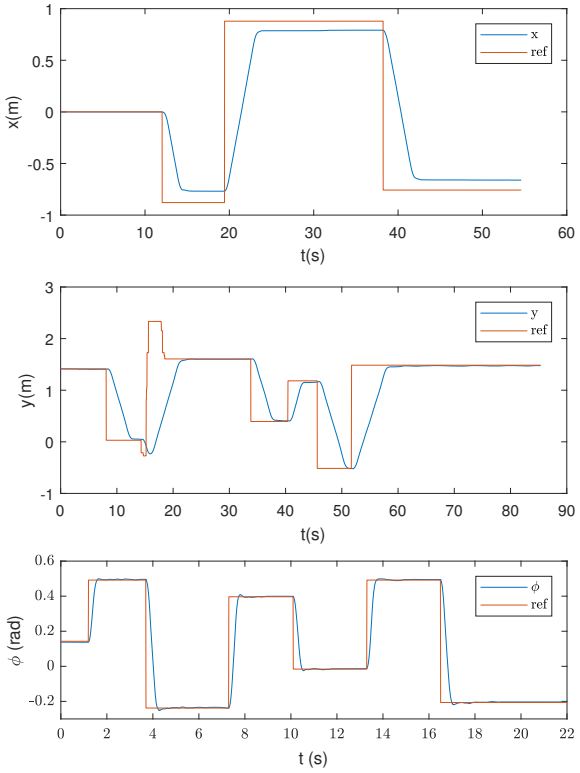

Fig. 5. x, y, & ϕ step responses

where $\underset{\rightarrow}{c}_k = \begin{bmatrix}c_k & c_{k+1} & \dots & c_{k+n_c}\end{bmatrix}^T$. The underlying closed loop nature of this controller does mean that constraints must be applied to the reference r_{k+1} in order to maintain feasibility of the QP, so a ramp limit is applied to the x and y setpoints in order avoid demanding an infeasible setpoint. No disturbance model is included at this time, however this could be included in future work at the cost of additional state dimensions.

V. Results

Performance was assessed by examining the ability of the platform to follow simple open-loop trajectories. Figure 5 shows the response of the x, y, and ϕ states to a number of step reference inputs. The y axis demonstrates good performance, with no overshoot, no offset, and good velocity constraint tracking. The x axis again shows good velocity constraint tracking and no overshoot, but exhibits a steady state error. The ϕ state shows a rapid rise time, minimal overshoot, and no steady state error.

Figure 6 shows the trajectory taken when following a square path with 1m sides whilst maintaining a constant yaw, with Figure 7 showing the individual θ_p, ϕ, $\dot{x}$, & $\dot{y}$ state trajectories over time for this path. This experiment again showed good performance in the y axis, but a steady state error in the x axis. The ϕ and θ_p states show minimal unwanted coupling with movements in the x and y directions, again indicating good performance. Figure 8 shows the trajectory when following a figure-of-8 path of 10s duration for four consecutive laps with a constant ϕ, with the individual x and y state trajectories shown in Figure 9. These results show

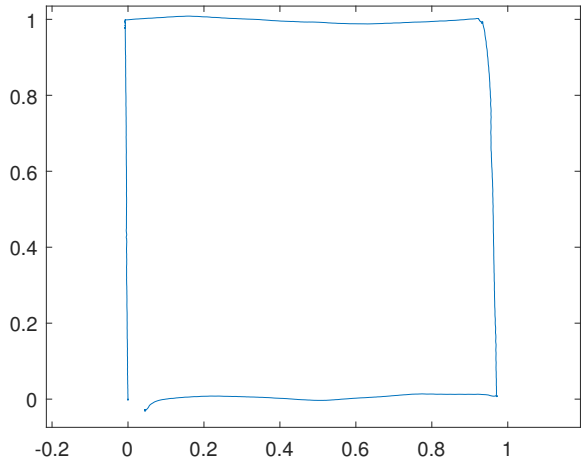

Fig. 6. Square trajectory tracking with constant yaw

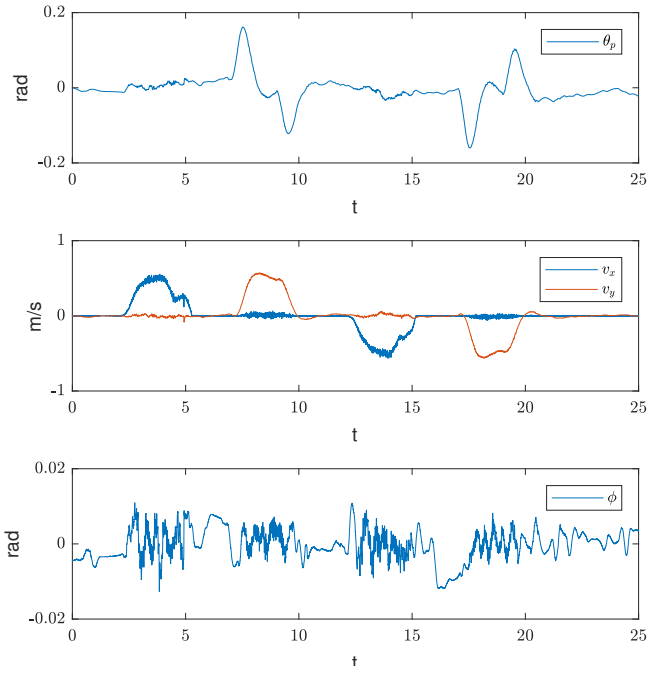

Fig. 7. Individual state trajectories for Figure 6

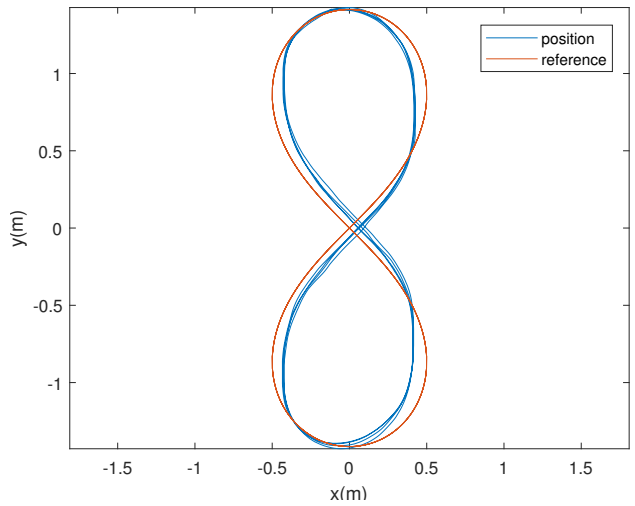

Fig. 8. Figure of 8 trajectory, four cycles of 10s duration

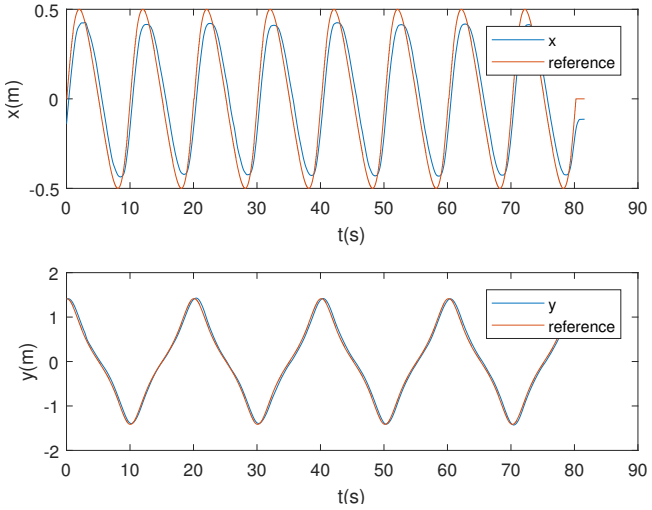

Fig. 9. Figure of 8 individual state trajectories

the platform has successfully demonstrated well controlled dynamically balanced omnidirectional motion, with minimal undesirable cross coupling between the x and θ_p, ϕ states. A steady state error is visible on the x state in all experiments due to the presence of friction in the Mecanum wheel bearings and the lack of controller integral action. This would be best addressed by the inclusion of this friction force into the dynamics model, however an integrating disturbance observer would also suffice.

VI. Conclusion

This paper has proposed a novel form of omnidirectional balancing platform, derived its inverse kinematic and dynamic models, and demonstrated the accuracy of this model by using it as the basis for a model-based predictive controller implemented on a proof-of-concept prototype. Experimental results show the prototype is capable of performing all of the motions required for it to fulfil the specification outlined in Section I.

References

[1] O. Boubaker, "The inverted pendulum: A fundamental benchmark in control theory and robotics," in International Conference on Education and e-Learning Innovations, July 2012, pp. 1–6.

[2] L. Bruzzone and G. Quaglia, "Review article: locomotion systems for ground mobile robots in unstructured environments," Mechanical Sciences, vol. 3, no. 2, pp. 49–62, 2012. [Online]. Available: http://www.mech-sci.net/3/49/2012/

[3] S. Kim and S. Kwon, "Dynamic modeling of a two-wheeled inverted pendulum balancing mobile robot," International Journal of Control, Automation and Systems, vol. 13, no. 4, pp. 926–933, Aug 2015. [Online]. Available: https://doi.org/10.1007/s12555-014-0564-8

[4] U. Nagarajan, G. Kantor, and R. Hollis, "The ballbot: An omnidirectional balancing mobile robot," The International Journal of Robotics Research, 2013.

[5] S. Reynolds-Haertle and M. Stilman, "Design and development of a dynamically-balancing holonomic robot."

[6] J. A. Rossiter, Model-based predictive control: a practical approach. CRC press, 2003.

[7] R. Siegwart, I. R. Nourbakhsh, and D. Scaramuzza, "Autonomous mobile robots," Massachusetts Institute of Technology, 2004.

[8] K. Zimmermann, I. Zeidis, and M. Abdelrahman, Dynamics of Mechanical Systems with Mecanum Wheels. Cham: Springer International Publishing, 2014, pp. 269–279.